# Highly Non-Linear Transport Across Single-Molecule Junctions via Destructive Quantum Interference

Julia E. Greenwald,[1] Joseph Cameron,[2] Neil J. Findlay,[2] Tianren Fu,[1] Suman Gunasekaran,[1] Peter J. Skabara,[2] Latha Venkataraman[1,3]

[1]Department of Chemistry, Columbia University, New York, New York, United States
[2]WestCHEM, School of Chemistry, University of Glasgow, Glasgow, United Kingdom
[3]Department of Applied Physics and Mathematics, Columbia University, New York, New York, United States

**To rival the performance of modern integrated circuits, single-molecule devices must be designed to exhibit extremely non-linear current-voltage (I-V) characteristics[1-4]. A common approach is to design molecular backbones where destructive quantum interference (QI) between the highest occupied molecular orbital (HOMO) and the lowest unoccupied molecular orbital (LUMO) produces a non-linear energy-dependent tunnelling probability near the electrode Fermi energy ($E_F$)[5-8]. However, tuning such systems is not straightforward, as aligning the frontier orbitals to $E_F$ is hard to control[9]. Here, we instead create a molecular system where constructive QI between the HOMO and LUMO is suppressed and destructive QI between the HOMO and strongly-coupled occupied orbitals is enhanced. We employ a series of fluorene oligomers containing a central benzothiadiazole[10] (BT) unit to demonstrate that this strategy can be used to create highly non-linear single-molecule circuits. Notably, we are able to reproducibly modulate the conductance of a six-nanometer molecule by a factor of more than $10^4$.**

Conduction in single-molecule circuits falls within the coherent electron transport regime when the device size is comparable to the electronic phase coherence length[11]. In this regime, delocalized MOs mediate charge transport, giving rise to non-linear Lorentzian resonances in the transmission spectrum. The energy-dependent transmission amplitude for a single MO, $j$, is described by the Breit-Wigner formula[12,13],

$$t_j(E) = e^{i\theta_j} \frac{\gamma_j}{E - \varepsilon_j + i\gamma_j} \tag{1}$$

where $\varepsilon_j$ is the energy of the MO and $\gamma_j$ is the coupling of the MO to the leads. The phase factor, $\theta_j$, describes the phase relation of the MO with respect to its overlap with states on either lead. The phase factor typically assumes values of 0 or π[14].

While individual resonances yield non-linear I-V characteristics, additional dynamic range can be gained by suppressing current flow at low bias through destructive QI. QI arises due to phase differences among the transmission amplitudes of multiple MOs[15,16]. In Fig. 1, we present two didactic examples of how destructive QI between two MOs, $j$ and $k$, can be achieved at $E_F$. Two MOs with the same phase ($\theta_j - \theta_k \approx 0$) and coupling ($\gamma_j \approx \gamma_k$) will exhibit destructive QI at $E_F$ if their energies straddle $E_F$ (Fig. 1a). Alternatively, two MOs of opposite phase ($\theta_j - \theta_k \approx \pi$) that are both lower (or equivalently both higher) in energy than $E_F$ (Fig. 1b) will exhibit destructive QI at $E_F$, provided the level farther from $E_F$ is better coupled to the leads. Notably, the latter type of destructive QI produces a steeper transmission function (Fig. 1c).

A common strategy to suppress low-bias current flow is to design molecular backbones where the HOMO and LUMO exhibit destructive QI near $E_F$[5-7,17], analogous to Fig. 1a. However, to effectively suppress transmission at $E_F$ and achieve a large non-linearity in the transmission spectrum, this strategy requires good alignment between $E_F$ and the transmission minimum, which can be difficult to achieve[9]. Moreover, this type of destructive QI is often implemented in small molecules[18] where through-bond tunnelling via σ orbitals is significant[19]. Therefore, transmission at $E_F$ is not adequately suppressed, and the dynamic range of such devices remains poor. In long molecular wires, where σ transmission is negligible, the small energy level spacing between MOs enables orbitals beyond the HOMO and LUMO to influence transmission at $E_F$[16,20]. Successive MOs of opposite phase (e.g., HOMO-1 and HOMO) can produce strong destructive QI at $E_F$, analogous to Fig. 1b. However, such destructive QI is typically accompanied by commensurate constructive QI between the HOMO and LUMO, which produces relatively flat transmission near $E_F$[21,22]. We demonstrate that constructive QI between the HOMO and LUMO can be suppressed and destructive QI between occupied Mos enhanced through molecular design using a series of three molecular wires comprising a central para-substituted BT unit flanked by fluorene arms on either side.

Fig. 2a shows the molecular structures of the systems investigated. Synthetic details are provided in Extended Data Fig. 1 and the Supplementary Information. The electron withdrawing BT unit localizes the LUMO and dictates its energy[10,23]. We use density functional theory (DFT) to calculate the MOs of **1**–**3** (see Methods). Figure 2b shows the LUMO is localized on the central BT unit, while the HOMO and HOMO-1 are delocalized across the backbone. The HOMO and HOMO-1 have opposite parity, which results in their having opposite phases of transmission. The DFT-calculated energy level diagrams (Fig. 2c) show near-uniform HOMO-LUMO gaps (~ 2.6 eV) across all three oligomers, in agreement with cyclic voltammetry data (Extended Data Fig. 2). Although there is a small shift in the oxidation peak, the reduction peak does not shift with length, confirming that the energy of the localized LUMO is dictated by the BT unit. The UV-Vis spectra (Fig. 2d) also show that the optical gap (~ 2.5 eV) does not vary with length, as indicated by the band at ~ 425 nm. The intensity of this band decreases with molecular length, suggesting reduced orbital overlap between the HOMO and LUMO as molecular length increases. The shorter wavelength band (~ 350 nm), which is characteristic of the oligofluorene unit[10], experiences a red shift as a function of molecular length, indicating an increased delocalization of the HOMO across the backbone from **1**–**3**. Thus, we expect transport in **1**–**3** will be coherent, mediated by the delocalized HOMO while the LUMO is effectively absent.

To measure the conductance of **1**–**3**, we use the scanning tunnelling microscope-based break-junction (STM-BJ) technique as described in the Methods section. We collect 2,600 STM-BJ traces and compile the traces into logarithmically-binned one-dimensional (1D) histograms (Fig. 3a). The most probable conductance values for each oligomer are determined by fitting each 1D histogram with a Gaussian. The conductance values, G, are then plotted against molecular length, L (S-to-S distance from DFT optimized structures), on a semi-logarithmic scale (Fig. 3a inset) and fit with an exponential, $G \sim e^{-\beta L}$. We obtain a decay constant, β, of 0.19 $Å^{-1}$, which is comparable to the decay constant observed for polyene[24] and other molecular wires[25,26] and suggests transport is coherent across all three oligomers (see Supplementary Fig. 1 for details). Since the applied bias (1.25 V) is smaller than the optical (Fig. 2d) and electrochemical gaps (~ 2.6 V) (Extended Data Fig. 2), transport is likely still in the off-resonant regime.

To confirm that junctions are formed by bridging the entire molecule between the two electrodes, we construct two-dimensional (2D) conductance-versus-displacement histograms. The 2D histogram for **3** is shown in Fig. 3b, with an individual conductance trace inset (see Supplementary Fig. 2 for 2D histograms for **1** and **2**). The observed junction elongation, ~ 6 nm, is consistent with the length of **3**. While the length of **3** approaches the length at which hopping transport becomes relevant[27], coherent transport has been observed in other systems of similar length[28,29]. Additionally, temperature-dependent measurements (Supplementary Fig. 3) show that conductance does not vary with temperature, consistent with a coherent transport mechanism.

Next, we measure the I-V characteristics of **1**–**3** (see Methods). Fig. 3c shows a 2D current versus time histogram for **3** (see Extended Data Fig. 3 for corresponding 2D histograms for **1** and

**2**). For each oligomer, traces in which the current exceeds 5 × $10^{-8}$ A at the maximum applied bias (± 2.0 V) are selected (~ 20% of traces). The cyclic I-V histograms show that junctions are stable for more than 1.7 s at room temperature in solution and do not rupture as the bias is repeatedly swept between ± 2 V at a rate of 20 V $s^{-1}$. The average I-V curves for **1**–**3** are all highly non-linear (Fig. 3d). (See Supplementary Fig. 4 for average I-V histograms for **1**–**3**.) The curve for **1** is uniformly steep on a logarithmic scale, whereas the curves for **2** and **3** manifest two distinct regions. At low bias, the I-V curves for **2** and **3** are linear because the through-molecule current is lower than the through-solvent current (Supplementary Fig. 5). Once the molecular junction current exceeds the solvent current, the I-V curves for **2** and **3** increase rapidly as the bias approaches ± 2 V, indicating that we may be approaching, but have not yet reached, the resonant transport regime. This is further corroborated by the numerical differential conductance curves, which do not show a peak within the bias range (Supplementary Fig. 6).

To highlight the stability of the junctions at high bias and the nonlinearity of transmission, we modify the STM-BJ measurement to enable rapid switching of the applied bias while holding the molecule in the junction (see Methods). Fig. 3e shows a 2D current-time histogram for bias switching measurements of **3** without data selection. (See Extended Data Fig. 4 for sample traces and Extended Data Fig. 5 for analogous histograms for **1** and **2**.) We observe high junction formation probabilities and large conductance ratios in the bias switching measurements of all three oligomers. The junction formation probabilities for **1**, **2** and **3** are 93%, 99% and 100%, respectively (Supplementary Fig, 7). In each of the six cycles, the molecule (**1**–**3**) is held at high bias for 12.5 ms without the junction rupturing, and in many traces, the current exceeds $10^{-7}$ A. The stability of the junctions at high bias indicates no irreversible changes occur, as might be expected when entering the resonant transport regime[30] or charging of the molecule in the hopping regime[31]. In many of the traces in Fig. 3e, the current at high bias (2.0 V) is more than 30,000 times larger than the current at low bias (0.5 V). Since the current at low bias is through-solvent rather than through-molecule current, we stress that 30,000 represents the lower bound of the enhancement factor and underscores the extreme nonlinearity of circuits formed with **3**.

We calculate transmission functions for junctions created with **1**–**3** (Fig. 4a) to elucidate the relationship between destructive QI and the non-linear I-V characteristics observed experimentally (see Methods for calculation details). The transmission functions show that, from **1** to **3**, the HOMO resonances shift closer to $E_F$ while the LUMO resonances shift farther from $E_F$. Thus, the transmission functions qualitatively agree with the optical and electrochemical data, insofar as the calculated HOMO-LUMO gap (~ 1.7 eV) does not vary significantly with molecular length. However, we note that these transmission functions do not capture the magnitude of the HOMO-LUMO gap accurately, due to errors inherent to DFT as discussed in Supplementary Information Section 4. Furthermore, despite the large applied bias, calculations including an applied electric field do not indicate a sizable Stark effect (see Supplementary Fig. 9).

Importantly, the DFT calculations demonstrate the LUMO is effectively decoupled in **1**–**3**. Fig. 4b shows that for all three oligomers, the HOMO and HOMO-1 are both more than an order of magnitude better coupled than the LUMO. In other highly conjugated systems, where the coupling of the HOMO and LUMO are similar, higher transmission is observed at low bias[22] due to constructive QI. In Fig. 4c, we overlay the HOMO resonance for **3** with a single-level model to show that, at $E_F$, DFT-based transmission, which accounts for all MOs, is 350 times lower than transmission assuming HOMO-dominated transport. Since the LUMO is decoupled, destructive QI among multiple pairs of resonances of opposite phase, e.g. HOMO–HOMO-1, HOMO-1–HOMO-2, etc., suppresses transmission near $E_F$. (See Extended Data Fig. 6 for visualization of destructive QI contributions.) The inset to Fig. 4c shows that such destructive QI increases with molecular length. To experimentally confirm that the LUMO does not contribute to transport within the applied bias range, we perform two-electrode electrochemical gating measurements of **1** (see Methods). These measurements demonstrate conductance is mediated by the HOMO (Supplementary Fig. 8) and the transmission function is quite asymmetric. By contrast, the LUMO is not decoupled in a control molecule lacking BT (Extended Data Fig. 7). Furthermore, two-electrode gating measurements of the control molecule suggest a more symmetric transmission function (Extended Data Fig. 8).

In conclusion, we have shown that constructive QI between the HOMO and LUMO can be suppressed in long molecular wires by decoupling the LUMO through chemical design. As a result, destructive QI between strongly-coupled occupied MOs of opposite parity gives rise to highly non-linear current-voltage characteristics. Notably, destructive QI increases as a function of molecular length because the energy level spacing between MOs decreases. Using this novel design strategy, we are able to modulate the conductance of a six-nanometer molecule by a factor of over $10^4$, suggesting a promising approach to developing functional, room temperature molecular electronics.

## References

1 Datta, S. *Quantum transport: atom to transistor*. (Cambridge University Press, 2005).

2 McCreery, R. L. & Bergren, A. J. Progress with Molecular Electronic Junctions: Meeting Experimental Challenges in Design and Fabrication. *Adv Mater* **21**, 4303-4322, (2009).

3 Cuevas, J. C. & Scheer, E. *Molecular electronics: an introduction to theory and experiment*. 2nd Edition. edn, (World Scientific, 2017).

4 Evers, F., Korytar, R., Tewari, S. & van Ruitenbeek, J. M. Advances and challenges in single-molecule electron transport. *Rev Mod Phys* **92**, (2020).

5 Baer, R. & Neuhauser, D. Phase coherent electronics: A molecular switch based on quantum interference. *J Am Chem Soc* **124**, 4200-4201, (2002).

6 Cardamone, D. M., Stafford, C. A. & Mazumdar, S. Controlling quantum transport through a single molecule. *Nano Lett* **6**, 2422-2426, (2006).

7 Andrews, D. Q., Solomon, G. C., Van Duyne, R. P. & Ratner, M. A. Single Molecule Electronics: Increasing Dynamic Range and Switching Speed Using Cross-Conjugated Species. *J Am Chem Soc* **130**, 17309-17319, (2008).

8 Yoshizawa, K. An Orbital Rule for Electron Transport in Molecules. *Accounts Chem Res* **45**, 1612-1621, (2012).

9 Guedon, C. M. *et al.* Observation of quantum interference in molecular charge transport. *Nat Nanotechnol* **7**, 304-308, (2012).

10 Belton, C. R. *et al.* Location, Location, Location - Strategic Positioning of 2,1,3-Benzothiadiazole Units within Trigonal Quaterfluorene-Truxene Star-Shaped Structures. *Adv Funct Mater* **23**, 2792-2804, (2013).

11 Gehring, P., Thijssen, J. M. & van der Zant, H. S. Single-molecule quantum-transport phenomena in break junctions. *Nature Reviews Physics* **1**, 381-396, (2019).

12 Breit, G. & Wigner, E. Capture of slow neutrons. *Phys Rev* **49**, 0519-0531, (1936).

13 Schuster, R. *et al.* Phase measurement in a quantum dot via a double-slit interference experiment. *Nature* **385**, 417-420, (1997).

14 Solomon, G. C. *et al.* Understanding quantum interference in coherent molecular conduction. *J Chem Phys* **129**, (2008).

15 Lambert, C. J. Basic concepts of quantum interference and electron transport in single-molecule electronics. *Chem Soc Rev* **44**, 875-888, (2015).

16 Gunasekaran, S., Greenwald, J. E. & Venkataraman, L. Visualizing Quantum Interference in Molecular Junctions. *Nano Lett* **20**, 2843-2848, (2020).

17 Hong, W. J. *et al.* An MCBJ case study: The influence of pi-conjugation on the single-molecule conductance at a solid/liquid interface. *Beilstein J Nanotech* **2**, 699-713, (2011).

18 Bai, J. *et al.* Anti-resonance features of destructive quantum interference in single-molecule thiophene junctions achieved by electrochemical gating. *Nat Mater* **18**, 364-369, (2019).

19 Garner, M. H. *et al.* Comprehensive suppression of single-molecule conductance using destructive sigma-interference. *Nature* **558**, 415-+, (2018).

20 Ke, S. H., Yang, W. T. & Baranger, H. U. Quantum-Interference-Controlled Molecular Electronics. *Nano Lett* **8**, 3257-3261, (2008).

21 Sedghi, G. *et al.* Long-range electron tunnelling in oligo-porphyrin molecular wires. *Nat Nanotechnol* **6**, 517-523, (2011).

22 Zang, Y. P. *et al.* Resonant Transport in Single Diketopyrrolopyrrole Junctions. *J Am Chem Soc* **140**, 13167-13170, (2018).

23 Wang, Y. & Michinobu, T. Benzothiadiazole and its pi-extended, heteroannulated derivatives: useful acceptor building blocks for high-performance donor-acceptor polymers in organic electronics. *J Mater Chem C* **4**, 6200-6214, (2016).

24 Gunasekaran, S. *et al.* Near Length-Independent Conductance in Polymethine Molecular Wires. *Nano Lett* **18**, 6387-6391, (2018).

25 He, J. *et al.* Electronic decay constant of carotenoid polyenes from single-molecule measurements. *J Am Chem Soc* **127**, 1384-1385, (2005).

26 Lafferentz, L. Conductance of a single conjugated polymer as a continuous function of its length (vol 322, pg 1193, 2009). *Science* **325**, 148-148, (2009).

27 Choi, S. H., Kim, B. & Frisbie, C. D. Electrical resistance of long conjugated molecular wires. *Science* **320**, 1482-1486, (2008).

28 Yamada, R., Kumazawa, H., Noutoshi, T., Tanaka, S. & Tada, H. Electrical conductance of oligothiophene molecular wires. *Nano Lett* **8**, 1237-1240, (2008).

29 Ashwell, G. J. *et al.* Single-molecule electrical studies on a 7 nm long molecular wire. *Chem Commun*, 4706-4708, (2006).

30 Fung, E. D. *et al.* Breaking Down Resonance: Nonlinear Transport and the Breakdown of Coherent Tunneling Models in Single Molecule Junctions. *Nano Lett* **19**, 2555-2561, (2019).

31 Schwarz, F. *et al.* Field-induced conductance switching by charge-state alternation in organometallic single-molecule junctions. *Nat Nanotechnol* **11**, 170-176, (2016).

**Acknowledgments.** J.E.G and S.G. are supported by NSF Graduate Research Fellowships under grant DGE-1644869. T.F. is supported by the NSF under award grant CHE-1764256. L.V. acknowledges financial support from the NSF under grant DMR-1807580. J.C., N.J.F. and P.J.S. thank the EPSRC for funding under grants EP/P02744X/2 and EP/N035496/2.

**Author Contributions.** J.E.G performed all STM measurements. J.C. and N.J.F synthesized all compounds. T.F. and S.G. carried out all calculations. J.E.G. and L.V. wrote the paper with contributions from all authors. L.V. and P.J.S. oversaw the project.

**Competing Financial Interests**. Authors declare no competing financial interests.

**Additional Information.** Supplementary information is available in the online version of the paper. Reprints and permission information is available online at www.nature.com/reprints. Correspondence and requests for materials should be addressed to L.V. and P.J.S.

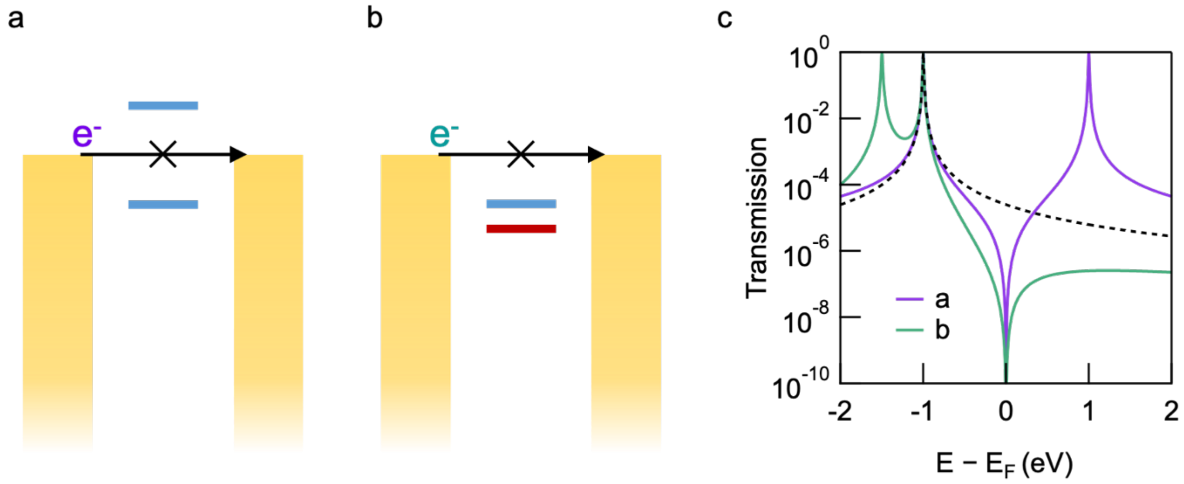

**Fig. 1. Destructive QI between two MOs at the Fermi energy, $E_F$. a,b)** Schematic illustrating QI with two levels. The MO phase for each level ($\theta_j$) is indicated by blue ($\theta_j = 0$) vs. red ($\theta_j = \pi$). **c)** Transmission functions corresponding to (a) and (b) calculated as $T(E) = |t_1 + t_2|^2$. Note in (a) the two levels straddle $E_F$ ($\varepsilon_{1(2)} = \pm\varepsilon_0$) and are equally coupled to the electrodes ($\gamma_1 = \gamma_2$), while in (b) the lower energy level ($\varepsilon_2 = 1.5\varepsilon_0$, $\gamma_2 = 1.5\gamma_0$) is better coupled than the higher energy level ($\varepsilon_1 = \varepsilon_0$, $\gamma_1 = \gamma_0$). A single-level model, calculated as $T(E) = |t_0|^2$ with $\varepsilon_0 = -1$ eV and $\gamma_0 = 0.005$ eV, is presented for comparison (dashed).

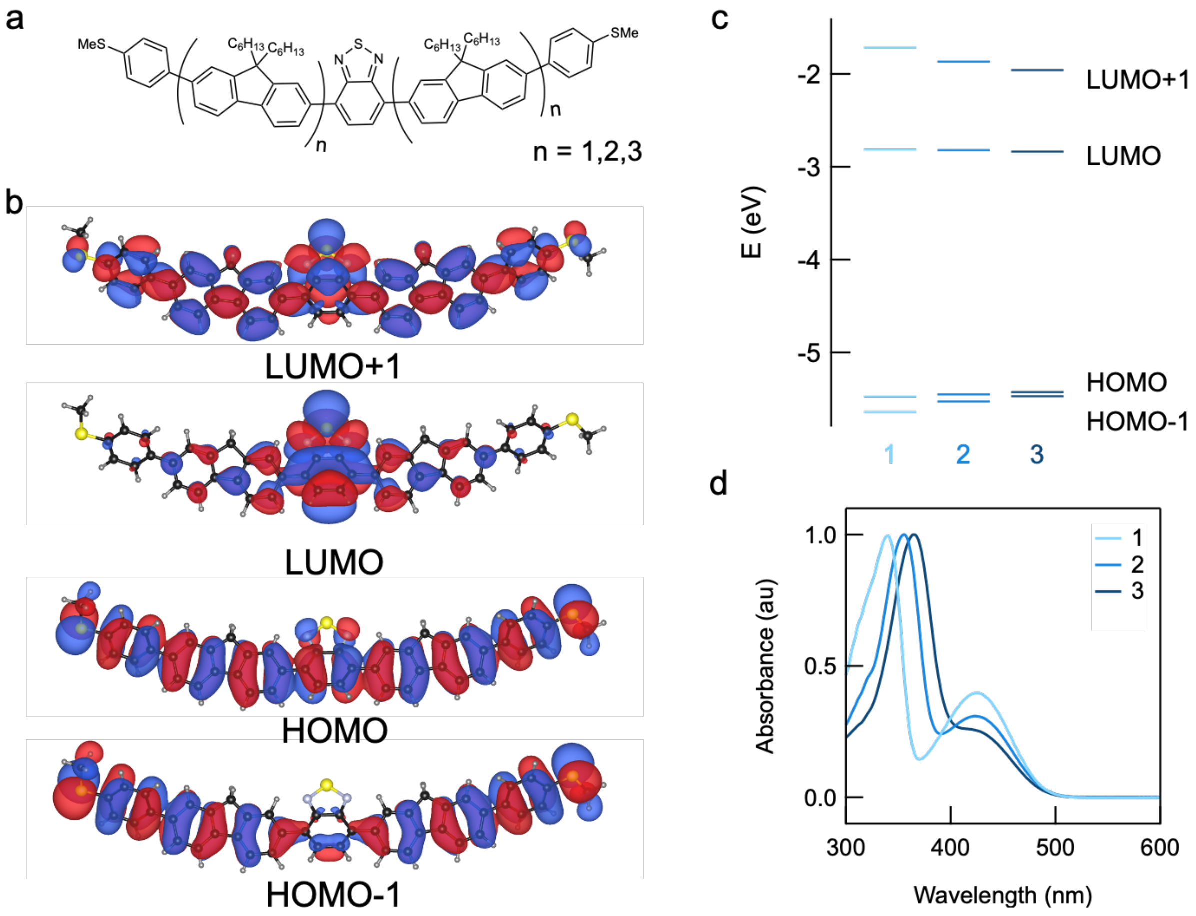

**Fig. 2. Structure and Electronic Properties of Molecules 1–3. a)** Molecular structure of **1**–**3**. The compounds **1**, **2** and **3** correspond to the number of fluorene units, n. **b)** MOs of **1** calculated using DFT with B3LYP functional. Note the HOMO and HOMO-1 have opposite parity, indicating their MO phase factors will be different. White, black, yellow, and light blue atoms represent H, C, S, and N, respectively. **c**) Energy level diagram for **1**–**3** constructed from DFT calculations. The energy gap between HOMO and HOMO-1 decreases with increasing molecular length. **d)** Normalised absorption spectra for **1**–**3** recorded in dichloromethane ($10^{-5}$ M).

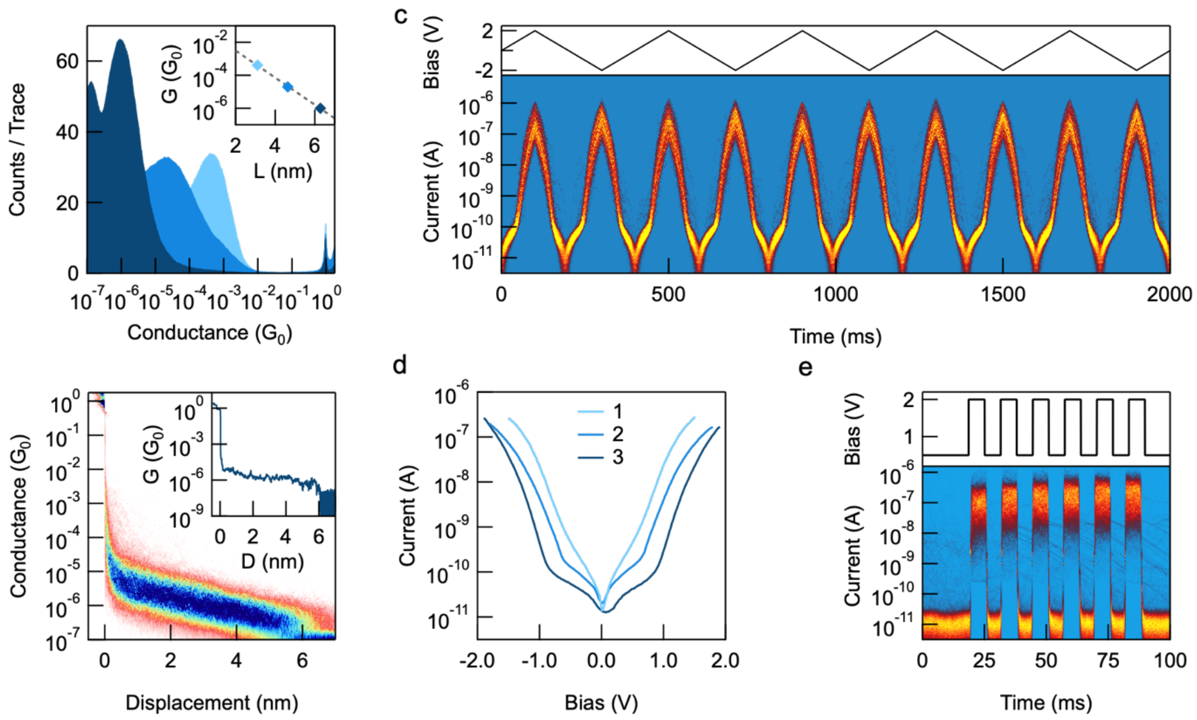

**Fig. 3. Conductance and Current-Voltage (I-V) Measurements of 1–3. a)** Logarithmically-binned 1D conductance histograms for **1**, **2** and **3**. Histograms are compiled from 2,600 STM-BJ traces collected using 1.25 V applied bias. The peak at $10^{-7}$ $G_0$ corresponds to the instrument noise floor. Inset: Conductance versus length for **1**–**3**. Fit line: $G \sim e^{-\beta L}$, where G is conductance, L is the DFT-based molecular S-S length, and $\beta = 0.19$ Å$^{-1}$. **b**) 2D conductance-displacement histogram and sample trace (inset) for **3**. Histogram is compiled from a subset of ~ 1,000 traces that evidence a plateau at 1 $G_0$. Counts increase from red to blue. **c)** Cyclic I-V measurements of **3.** Top: Bias applied across the junction with a 100 kΩ resistor in series while tip-substrate gap is held constant. Bottom: 2D current-time histogram constructed from 282/1,000 traces (see Extended Data Fig. 3 for cyclic I-V histograms for **1** and **2**). **d)** Average I-V curves for **1**–**3** generated by fitting cyclic I-V histograms (see Supplementary Fig. 4 for corresponding average I-V histograms). **e)** Bias switching measurements of **3**. Top: Bias applied across the junction with a 100 kΩ resistor in series while tip-substrate gap is held constant. Bottom: 2D current-time histogram compiled from 1,046

traces measured consecutively (54 traces where no gap formed during the hold were excluded). Counts increase from dark red to yellow in (c) and (e).

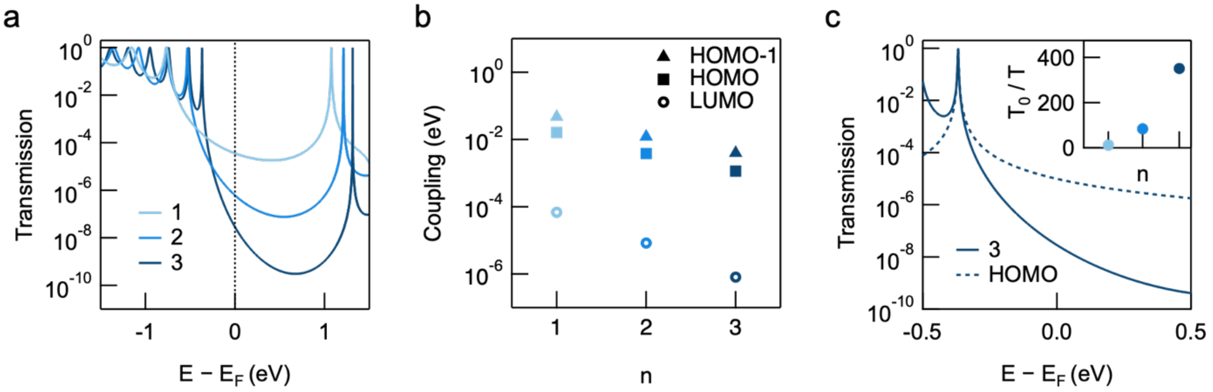

**Fig. 4. Transmission Function Calculations for Au-Molecule-Au Junctions. a)** Transmission functions for molecular junctions of **1**–**3** calculated using DFT. **b)** Coupling between MO and leads for **1**–**3**. Coupling values extracted from DFT-based transmission calculations. **c)** Transmission function of **3** (solid line) overlaid with a single-level model of the HOMO (dashed). Inset: Ratio of transmission at $E_F$ for single-level model of HOMO, $T_0$, to DFT-based transmission, T, for **1**–**3.** The increase in $T_0/T$ indicates destructive QI increases with molecular length. See Extended Data Fig. 9 for analogous overlays for **1** and **2**.

## Methods

**Conductance Measurements.** The STM-BJ technique has been described previously[32,33]. In brief, we prepare ~ 30 µM solutions of **1**, **2** and **3** in UV-treated 1-bromonaphthalene (see Supplemental Information Section 5 for solvent details). The solution is deposited on an Au-coated steel substrate. An Au tip is then repeatedly brought into contact with and retracted from the substrate. As the tip is retracted, an atomic point contact forms, and subsequently breaks, yielding a nanometer-scale gap. The terminal thiomethyl linkers of **1**–**3** bind to the tip and substrate, forming an Au-molecule-Au junction. As the tip is retracted further, the junction breaks once the gap is too large for the molecule to bridge. A bias is applied across the tip/sample junction with a 200 kΩ resistor in series with the junction. The current and voltage measured across the junction are recorded as a function of tip displacement to generate conductance (G = I/V) versus displacement traces. The conductance of the atomic point contact is roughly 1 $G_0$ ($G_0 = 2e^2/h$). Plateaus at conductance values lower than 1 $G_0$ in the conductance versus displacement traces indicate the formation of molecular junctions. For the two-electrode gating experiments[34], a coated STM tip and 100 kΩ series resistor are used. Conductance measurements of **1** and **C1** are performed in ~ 40 μM solutions of propylene carbonate with added supporting electrolyte (~ 0.1 M $TBAPF_6$).

**Current-Voltage Measurements.** I-V characteristics of **1**–**3** are measured by withdrawing the tip at a rate of 16 nm $s^{-1}$ to form a gap between the tip and substrate while applying a bias of 0.1 V. The tip is then held in a fixed position as the bias is ramped continuously at a rate of 20 V $s^{-1}$ for five cycles (for **1**, the bias was ramped from +1.8 V to -1.8 V, while for **2** and **3** from +2.0 V to -2.0 V). The tip is then further withdrawn at a rate of 16 nm $s^{-1}$ to rupture the junction. All biases are applied across the junction using a 100 kΩ resistor in series with the junction. Traces are selected where the current exceeds $5 \times 10^{-8}$ A at the maximum applied bias (i.e. ± 1.8 V for **1** and ± 2.0 V for **2** and **3**), and histograms are constructed from the hold portion of each selected trace. 2D current versus time histograms are constructed using logarithmically binned current (57 bins $dec^{-1}$) and linearly binned time (4000 bins $s^{-1}$). Average 2D current versus voltage histograms are constructed from the hold portion of each trace using logarithmically binned current (57 bins $dec^{-1}$) and linearly binned voltage (100 bins $V^{-1}$). Average I-V curves are generated by fitting the current data in each voltage bin with a Gaussian. Since the series resistor reduces the voltage applied across the junction when the current exceeds ~ $2.5 \times 10^{-7}$ A, the highest positive bias portions of the average I-V curves are omitted (i.e., max bias for **1** is ± 1.5 V, max bias for **2** is ± 1.8 V, max bias for **3** is ± 1.9 V).

**Bias Switching Measurements**. Instead of continuously retracting the tip from the substrate, the tip is withdrawn at a rate of 16 nm $s^{-1}$ to form a molecular junction. The tip is then held in a fixed position while the applied bias is pulsed between a high and low value for six cycles (lasting 100 ms). Finally, the tip is withdrawn again at the same rate to rupture the junction. The bias is applied across the junction using a 100 kΩ resistor in series with the junction. For **1** and **2**, the applied high bias is 1.5 V. For **3**, the applied high bias is 2.0 V. For all three, 0.5 V is applied while pulling and during the low bias portion of the hold.

**DFT Calculations**. Density functional theory (DFT) simulations are conducted with the FHI-AIMS package[35,36] using the B3LYP and PBE exchange-correlation functionals[37] for the isolated molecule and transmission calculations, respectively. For each molecule, we first optimize the structure (alkyl chains are replaced with hydrogens to facilitate computation) with a maximum residual force per atom of $10^{-2}$ eV·Å$^{-1}$. For the transmission calculation, the optimized structure is used to construct an $Au_1$-molecule-$Au_1$ structure which is relaxed to determine the optimal Au-S bond length and orientation. Two tetrahedral $Au_{60}$ clusters are then added, maintaining the optimal Au-S bond. The $Au_{60}$ clusters have (111) lattice surfaces and represent the gold electrodes in the single-molecule junction. We use the $Au_{60}$-molecule-$Au_{60}$ structure to calculate the energy-dependent transmission function of the molecule. The transmission functions are calculated with the AITRANSS package based on a non-equilibrium Green's function formalism[38,39].

**Data Availability.** Data associated with the synthesis and characterisation of **1**–**3** and **C1** are available at http://dx.doi.org/10.5525/gla.researchdata.1062. Additional data that support the findings of this study not included in the supplementary information document are available from the corresponding authors upon reasonable request.

**Code Availability.** The data that support the findings were acquired using a custom instrument controlled by custom software (Igor Pro, Wavemetrics). The software is available from the corresponding author upon reasonable request.

## References

32 Xu, B. Q. & Tao, N. J. J. Measurement of single-molecule resistance by repeated formation of molecular junctions. *Science* **301**, 1221-1223, (2003).

33 Venkataraman, L., Klare, J. E., Nuckolls, C., Hybertsen, M. S. & Steigerwald, M. L. Dependence of single-molecule junction conductance on molecular conformation. *Nature* **442**, 904-907, (2006).

34 Capozzi, B. *et al.* Single-molecule diodes with high rectification ratios through environmental control. *Nat Nanotechnol* **10**, 522-U101, (2015).

35 Koentopp, M., Burke, K. & Evers, F. Zero-bias molecular electronics: Exchange-correlation corrections to Landauer's formula. *Phys Rev B* **73**, (2006).

36 Blum, V. *et al.* Ab initio molecular simulations with numeric atom-centered orbitals. *Comput Phys Commun* **180**, 2175-2196, (2009).

37 Perdew, J. P., Burke, K. & Ernzerhof, M. Generalized gradient approximation made simple. *Phys Rev Lett* **77**, 3865-3868, (1996).

38 Arnold, A., Weigend, F. & Evers, F. Quantum chemistry calculations for molecules coupled to reservoirs: Formalism, implementation, and application to benzenedithiol. *J Chem Phys* **126**, (2007).

39 Bagrets, A. Spin-Polarized Electron Transport Across Metal-Organic Molecules: A Density Functional Theory Approach. *J Chem Theory Comput* **9**, 2801-2815, (2013).